Aerosol Generated Core-shell Nanoparticles

Synthesis and Characterization

Snellman, Markus

Aerosol Generated Core-shell Nanoparticles

Synthesis and Characterization

Licentiate Thesis

Markus Snellman

Supervisor: Knut Deppert
Co-supervisors: Maria E. Messing, Namsoon Eom, Martin Ek, Rasmus Westerström
Opponent: Prof. Viveka Alfredsson
Examiner: Assoc. Prof. Martin Magnusson

LUND
UNIVERSITY

Division of Solid State Physics
Department of Physics
Lund University
June 2021

Abstract

Aerosol technology is a promising platform to synthesize and study core-shell nanoparticles – a multi-elemental nanoparticle system where the core of one material is covered by a shell of another material. In this thesis, two distinctly separate strategies have been explored to synthesize core-shell nanoparticles by aerosol methods: physical vapor deposition (PVD) by evaporation, and surface segregation via thermal treatment.

Using a novel aerosol PVD design with a local heater to decouple shell material heating from the aerosol, Zn condensation on Au core particles was studied and compared to a simple model based on kinetic gas theory and Comsol simulations. Elemental characterization with electron microscopy did, however, reveal an AuZn alloy instead of the intended core-shell morphology. Growth was additionally found to be limited by homogenous nucleation of Zn vapor.

In contrast, tube furnace heating of spark discharge generated CuAg agglomerates demonstrated the possibility to obtain both a quasi-Janus and a core-shell nanoparticle morphology, simply by tuning the furnace temperature to control the surface segregation. The chemical composition of core and shell phases determined by machine learning algorithms applied to elemental maps of the particles were in congruence with X-ray Photoelectron Spectroscopy measurements. Further elemental characterization of the spark discharge generated CuAg particles revealed a low inter-particle compositional variance, the reason of which remains to be investigated.

Contents

List of publications

The thesis is partly based on the following publication:

I.
Continuous gas-phase synthesis of core–shell nanoparticles *via* surface segregation
Markus Snellman, Namsoon Eom, Martin Ek, Maria E. Messing, Knut Deppert. Nanoscale Advances (2021).

Acknowledgements

Writing this thesis has been much easier than I thought, thanks to the great people in our research group. Knut, thank you for offering me this position and for mentoring me throughout these last couple of years. It has been great being able to share my struggles and ideas, no matter how far-fetched.

Thank you Maria for co-supervising me and leading the aerosol group. You always challenge me to think ahead and not jump to conclusions. You and Knut's extensive knowledge and contacts in the field of aerosol technology are of great importance for the group. Being able to "cry out" about my scientific worries to you has been really valuable.

Namsoon, it has been great working on projects together and writing this first manuscript. I hope there will be many more, and I hope I will be able to catch up to you in the field of molecular dynamics and Monte Carlo simulations.

Martin, thank you for sharing your extensive knowledge on electron microscopy, and treatment of related spectroscopy methods. You have opened my eyes to the "data science" of spectroscopy.

I don't know a lot about X-ray techniques, but the little I do know I attribute to Rasmus. Having been able to do measurements at MAX IV has been a great experience. I'm positive we can do more and better of these types of measurements.

Then, I'd like to acknowledge the rest of the aerosol group. Martin M. always has interesting suggestions and insights during our meetings. Without Bengt I would likely not have gotten any work done, so thank you Bengt for being the tech muscle of the group. Calle and Sara, thank you for teaching me everything related to the aerosol lab and letting me bug you with basic questions at any time. I look forward to do collaborative projects later on. Sudha, I really enjoyed doing the aerosol technology course together, and I wish you good luck with your contemporary thesis work. Pau, Marie, Mehran, Linnéa and Sara B: it has been great getting to help you a little bit in the lab, and extra thanks to Marie and Sara B for helping me out with microscopy and XRD respectively.

Apart from the aerosol group, I have also had the opportunity to do some collaborations with people at other departments. I want to thank Michael for giving my generated nanoparticles a purpose in catalytic crystal growth. It has been really interesting discussing different experimental ideas and approaches, and not least having been able to participate in environmental-TEM experiments! Per, while I only got to work with you a little with, I am amazed by the interesting investigations you do in the lab and I'm thankful I got to see some of it.

Last but not least, I want to thank my lovely "sambo" Andrea, and our families – the most important people in my life – without whom I would not have been able to complete this thesis.

Introduction

1.1 Nanoparticles

Nanoscience or nanotechnology can, in broad terms, be said to be the manipulation of atomic and molecular to nanoscaled structures, with at least one dimension smaller than 100 nm. One of the most fundamental nanostructures are nanoparticles (NPs): objects with all physical dimensions smaller than 100 nm [1]. On this length-scale, NPs may bridge the properties between atomic or molecular structures and bulk materials [2], where the NPs' properties generally diverge more from their bulk counterparts with decreasing sizes. These often exotic properties are leveraged in a diverse range of applications. The high surface-to-volume ratio makes NPs very effective in catalysis [3]; bio-compatible NPs are utilized in cancer detection and treatment [4], and quantum confinement effects lend NPs tunable optical properties [5] with applications in, e.g., optoelectronics and biomedicine.

Considering the broad scope of NP applications, there is a demand for accurate synthesis of engineered NPs with tailored size, shape and composition. We can crudely divide synthesis routes after the physical phases of the surrounding medium: the solid phase, the liquid phase and the gaseous phase. A subset of gas-phase synthesis techniques is the production and manipulation of NPs in the aerosol phase, i.e., a NP-gas suspension, which has been the methodology used in this thesis.

1.1.1 Aerosol nanoparticles

An aerosol is a suspension of microscopic liquid or solid particles in a gas. Everyday examples include byproducts from natural phenomena, such as fire smoke, salt particles from ocean sprays and atmospheric water droplets in clouds [6, p. 1].

Deterministic synthesis of engineered aerosol NPs has been researched for decades. The aerosol route of producing NPs has the benefit of being continuous and solvent free. If gaseous precursors are not used, these methods produce minimal waste products, in stark contrast to chemical solvent synthesis. Indeed, ablating bulk materials into NPs in a top-down fashion is attractive in its potential simplicity, and has been the main strategy for aerosol generation in our group by means of thermal evaporation [7] and

spark ablation [8], the latter of which has been the method used for creating NPs in this work.

The continuous aspect of aerosol NP generation cannot be stressed enough. Suspending NPs in the gas phase allows for continuous manipulation via sophisticated aerosol technology tools for electric charging, size filtering and counting of the particles. Choosing a desired particle size (within certain limits) is as easy as flicking a switch. Coupling the size selected particle flow to a furnace allows for online and unsupported sintering and evaporation investigations of NPs.

1.1.2 Core-shell aerosol nanoparticles

Further opportunities for aerosol NP manipulation and characterization seem limited only by imagination. Recent works have, for instance, implemented in-flight Raman spectroscopy [9] of and physical vapor deposition (PVD) onto the suspended NPs [10]. The latter is an interesting approach for making a promising, yet in aerosol synthesis relatively unexplored, subset of NPs: core-shell NPs.

A core-shell NP consists of a core particle of one material covered by a shell of another material. The interest in this morphology stems from the possibility to combine properties of separate materials or to achieve enhanced properties in synergistic material effects. As an example, capping a semiconductor core particle with a shell of a wider bandgap semiconductor improves the core material's photo-luminescence and quantum yield [11]. Passivating a magnetic core with a biocompatible shell has important applications as MRI contrast agents and for targeted cancer therapy [12]. In catalysis, where the surface composition is the most important catalyst property, the use of expensive noble metals can be reduced by having a cheap core supporting the catalytically active shell [13].

1.2 Motivation and outline of thesis

As mentioned, a strategy for continuous synthesis of core-shell NPs is depositing a shell onto the suspended core particles via some PVD method. In low pressure condition synthesis, such as inert gas condensation, sputtering a shell onto core NPs has successfully yielded high-quality core-shell and core-multishell particles [14, 15]. Implementing similar approaches for aerosol synthesis is attractive due to the obvious benefits of reduced process complexity, including avoiding strict vacuum control and cleaning protocols.

The goal of this thesis has been to develop a methodology for continuous aerosol synthesis of core-shell NPs. One applied strategy has been the implementation of a custom evaporator, described in Sec. 2.2.3, to deposit a shell material onto core particles generated by spark ablation, described in Sec. 2.1. To this end, Au core NPs were generated by spark ablation, and Zn was evaporated as a shell material due to its high vapor pressure at relatively low heating temperatures. A simple model based on kinetic gas theory and Comsol modelling of the PVD chamber (Sec. 2.2.4) is compared to the experimental results in Sec. 2.2.3 and Sec. 3.2.

The complexity of a secondary PVD coating step can be avoided by clever NP material combinations. Mixing particles of immiscible materials with different surface energies can be a viable route to attain core-shell NPs via thermal induced surface segregation (discussed in Sec. 3.4 and Paper I), which has been another avenue investigated within this work. The system studied here has been CuAg NPs, generated by two separate, pure Cu and Ag electrodes in the spark discharge generator. Electron microscopy and elemental characterization (Sec. 3.1 and 3.2) have been important techniques to characterize these structures; using machine learning techniques, extraction of chemical phases from elemental data (Sec. 3.2.1) is compared to X-ray Photo-electron Spectroscopy (Sec. 3.3).

Aerosol nanoparticle generation, modification and on-line characterization

2.1 The spark discharge generator

Spark ablation, conceived in 1988 by the authors in Ref. [16], has shown to be a viable technique for large-scale, high-purity generation of aerosol NPs [17]. The basic setup consists of a high-power, high-voltage source charging a capacitor bank (capacitance C being typically 10 nF to 100 nF) with a charging current I (ca. 1 mA to 50 mA), shunted to two conducting electrodes separated by a gap of a few mm (see schematic in Fig. 2.1). At a high enough voltage, the atmosphere between the electrodes breaks down into a conducting plasma that the capacitor bank discharges its energy through, ablating material from the electrodes' surfaces. Often termed spark ablation, we will call the system/process spark discharge generator/generation (SDG) in this thesis.

Although conceptually a simple setup, there are several intricacies to the process conditions and especially the physics behind the NP generation, a few of which will be briefly mentioned here. During the capacitor bank discharge, the current will oscillate back and forth between the electrodes, as the equivalent electrical circuit can be modelled as an underdamped RLC-circuit. It is often reported that the heat of the plasma, having temperature between 10 000 K to 30 000 K [18, 19], drives the erosion (evaporation) of the electrodes. Simultaneously, ionic bombardment lead to atom ejection from the electrode surfaces [20, 21].

The ion-bombardment and evaporation create hot, supersaturated vapors of electrode atoms, that due to rapid quenching in the surrounding carrier gas [10] nucleate into singlet NPs, on the single-nanometer range. Collisions between singlets can lead to complete coalescence as heat released from the reduction in surface area raises the particle temperature [22]. At some critical size, further collisions between the primary particles lead to non-complete coalescence and the product in most cases are polydisperse fractal-like agglomerates, due to the fast coagulation rate [23]. The ablated material

(agglomerates) is subsequently transported with a carrier gas downstream the aerosol circuit.

One of the most attractive benefits of SDG is the flexibility in choice of electrode material: virtually any conducting material can be used, and SDG has been used to synthesize monometallic NPs [8, 19], bimetallic NPs [21, 24], semiconducting NPs [25] and metallic-semiconducting mixed NPs [26]. As the current (and voltage) oscillates back and forth, energy oscillates too, alternating the electrode being ablated. The oscillating nature of the discharge is a crucial feature to obtain mixed particles when working with electrodes of separate materials. This enabled the generation of mixed CuAg NPs in this work by using one pure Cu electrode and one pure Ag electrode.

2.2 Extended aerosol setup

In many applications, we want monodisperse quasi-spherical NPs, a far cry from the typical SDG product. To accomplish this we use common aersol tools as depicted in Fig. 2.1. This section will describe their function and uses.

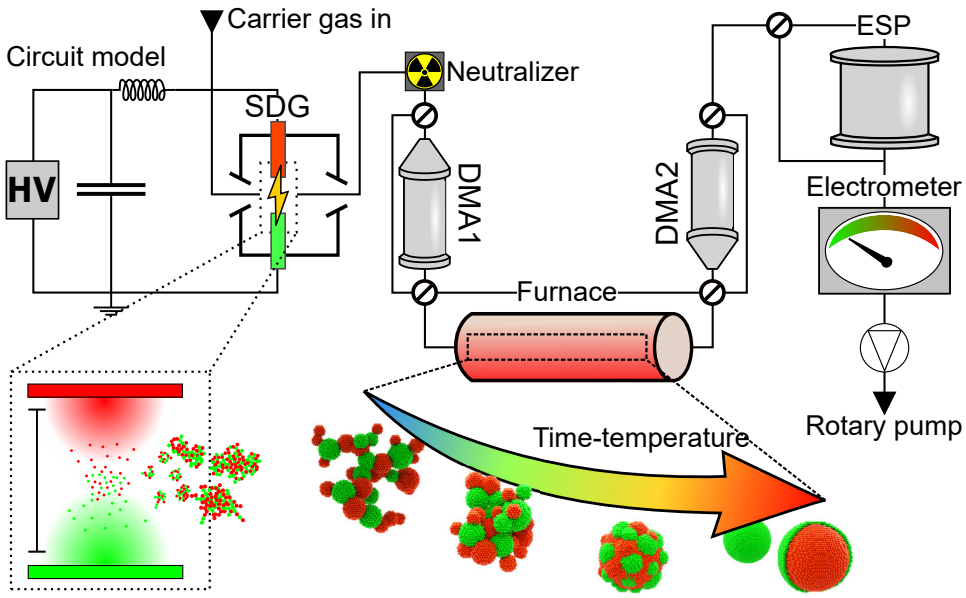

Figure 2.1: Experimental setup with equivalent circuit model for the SDG and schematic of the aerosol circuit and instrumentation.

2.2.1 Charging, size selection, counting and deposition

The primary tool to size-select NPs from a polydisperse aerosol is the Differential Mobility Analyzer (DMA). It filters particles based on their electrical mobility: the ability to move in an electric field [6, p. 322], which is proportional to ne/d_m, where ne is the number of elementary charges attached to the particle and d_m is the particle mobility equivalent diameter. Before size selection, we assign a known charge-distribution, an equilibrium Boltzmann distribution, using a neutralizer: a radioactive source (Ni^{63}) that emits beta radiation and charges the aerosol within about a couple of seconds [6, p. 335-338]. Note that for agglomerates, d_m is the diameter of a *spherical* particle with equivalent electrical mobility. In the case of spherical particles, d_m and the geometric particle diameter d_p coincide [27].

Essentially, the DMA is a parallel plate capacitor where particle penetration is controlled by the electric field. In a cylindrical DMA, which is the type used here, the electric field is applied between two concentric cylinders: the outer cylinder is grounded and a bias is applied to the inner cylinder. The polydisperse aerosol flow Q_a is let in close to the outer cylinder and a sheath flow Q_{sh} is let in in the center, between the electrodes. Particles with too high electrical mobility either deposit on the inner or the outer electrodes, depending on their polarity. Uncharged particles and particles with too low electrical mobility are swept out with the sheath flow, whereas particles within a certain electrical mobility range (resolution) exit the DMA as a monodisperse aerosol. It can be shown that the resolution (FWHM) of the DMA is Q_a/Q_{sh} [28]. In our setup, $Q_a = 1.68\,\mathrm{L\,min^{-1}}$ and $Q_{sh} = 10\,\mathrm{L\,min^{-1}}$ so the resolution is about $d_p \pm 1/6 \times d_p$, for spherical particles of diameter d_p.

To achieve a specific number or concentration of deposited aerosol NPs on a substrate, we require information on their concentration in the carrier gas. The charges attached to the NPs can be utilized to count them with an electrometer. The electrometer samples the particles on a filter and measures the induced current, which is directly proportional to the charged particle concentration [29].

With a known carrier gas NP concentration, one can easily estimate the particle surface concentration when depositing on a substrate. In our setup, an electrostatic precipitator (ESP) has been used, which enables highly efficient deposition of charged sub-micron particles [30]. An ESP takes in the aerosol flow and uses a strong electric field to deposit the particles on

virtually any substrate supported on a biased plate. The concentration of deposited spheroid NPs on the substrate can be calculated, assuming 100% collection efficiency and laminar aerosol flow in the ESP, using the Preger equation [31]:

$$c_{surf} = t c_{gas} E Z_p \tag{2.1}$$

where t is the deposition time, c_{gas} is the particle concentration in the carrier gas, E is the electric field strength and Z_p is the particle electrical mobility.

2.2.2 Thermal reshaping

To reshape the fractal-like agglomerates exiting the SDG into spheroid NPs, we use a tube furnace. Heating the agglomerates will lead to sintering, or compaction as often termed in aerosol technology. Compaction is driven by atomic diffusion that depends on temperature and diffusion mechanism. For aerosol NPs, it is believed that surface diffusion is the dominant mechanism as surface atoms can more easily diffuse than atoms in the bulk of the particles [28]. After some time-temperature history in the furnace, the agglomerates can be compacted such that a higher temperature will not decrease their mobility diameters further, and the particles are essentially spherical. Beyond this compaction temperature T_c, internal restructuring may take place; for instance, grain growth leads to increased crystallinity of the particles and particle mass can decrease due to evaporation [32].

Positioning the furnace between two DMAs in a so-called tandem-DMA setup allows us to study the compaction process directly in the aerosol phase. Setting the first DMA (DMA1) to a fixed mobility diameter and scanning the mobility size distribution in the second DMA (DMA2) after the aerosol has passed the tube furnace, enables tracking the evolution of the aerosol mobility size distribution as a function of temperature. It is common to study the change in the mean or mode of the distribution.

Consider the compaction of CuAg aerosol NPs, shown in Fig. 2.2, where DMA1 has been set to a fixed mobility diameter of 35 nm. At room temperature, the mobility diameters in DMA1 and DMA2 coincide, but as the furnace temperature increases, the peak mobility diameter decreases in DMA2 as compaction initiates. In Fig. 2.2, this occurs already at 100 °C. For many aerosol materials, especially noble metals, full compaction can be seen as a sudden drop in mobility diameter, followed by a mobility diameter plateau where full compaction has been reached [33]. Beyond T_c, evaporation can be detected with continuously decreasing mobility diameter as function of temperature.

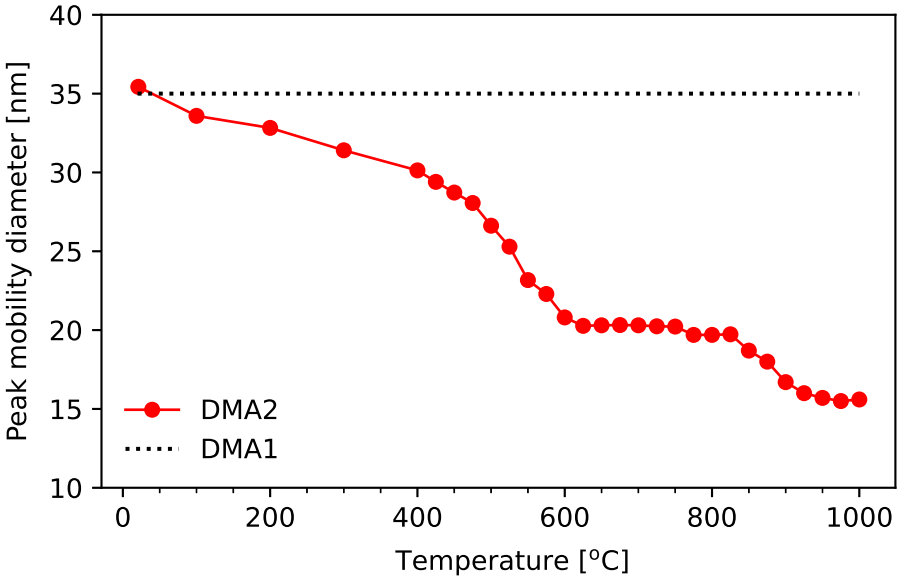

Figure 2.2: Compaction curve of CuAg aerosol particles.

Fig. 2.2 shows a rapid drop in the CuAg compaction curve at about 500 °C. At a temperature of about $T_c = 600\,°C$, a mobility diameter plateau is reached, where the particles are fully compacted. Beyond 900 °C, the mobility diameter decreases again, which can likely be attributed to Ag evaporation. Ag evaporation can qualitatively be described with the Knudsen equation for the evaporation rate of an element:

$$\frac{J_{ev}}{A} = \frac{p_v}{\sqrt{2\pi mkT}} \tag{2.2}$$

where J_{ev}/A is the evaporation rate per unit area at temperature T, p_v and m are the vapor pressure and the atomic mass of the material, and k is Boltzmann's constant. The area normalized evaporation rate is plotted for a few materials using vapor pressure data from Ref. [34] in Fig. 2.3.

The evaporation rate of Ag is significantly higher than that of Cu, as seen in Fig. 2.3 (note the log-scale), which may explain the mobility diameter drop in Fig. 2.2 at ca. 900 °C. Ag evaporation is further corroborated by elemental quantification of the NPs in Sec. 3.2. Increasing the tube furnace temperature further would eventually increase the evaporation of Cu as well, leading to a hefty material loss from the NPs and rapid decrease in mobility diameter.

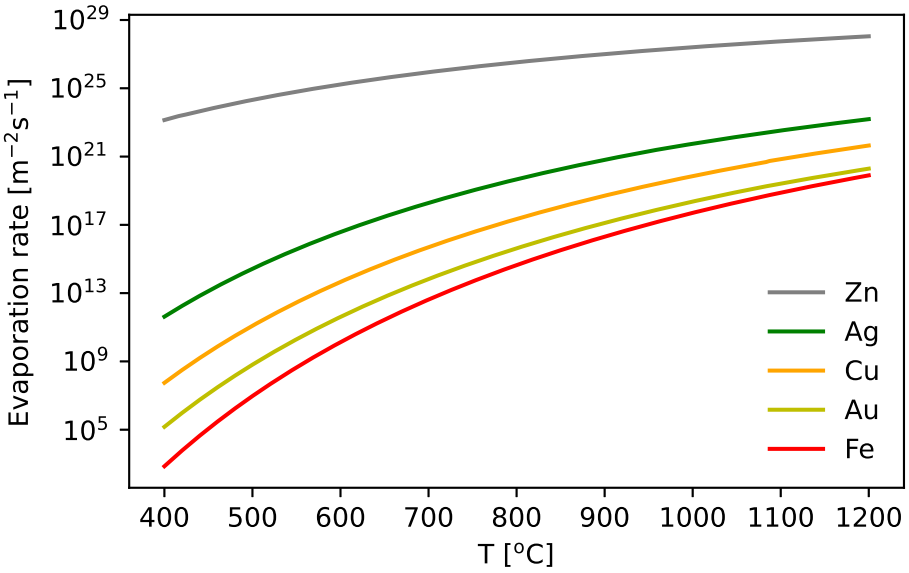

Figure 2.3: Evaporation rate of Zn, Cu, Ag, Au and Fe.

2.2.3 PVD: thermal evaporation

One rational extension to the aerosol circuit in Fig. 2.1 to synthesize core-shell NPs is a PVD chamber to evaporate a shell material onto compacted core NPs. Previous works in online aerosol PVD to create inorganic core-shell NPs have utilized a coating step with spark ablation [10] and furnaces [35, 36, 37]. Simultaneously, growth of aerosol NPs by condensation is an important technique for particle detection in concensation nuclei counters [6, p. 292-294].

Spark ablation coating of core NPs is an interesting approach, but it seems the high supersaturation of the ablated vapors and the non-continuous discharging lead to core NP decoration of smaller particles instead of a coherent shell [10]. Karlsson et al. [35] used a separate tube furnace to coat size-selected, compacted Au particles with Ga by evaporation. The shell growth, studied by a separate DMA, was controllable up to a certain evaporation temperature after which homogenous nucleation of Ga decreased the shell growth rate.

A more sophisticated evaporator implementation by Harra et al. [36] used a sectional tube-furnace with two *additional* tube furnaces to minimize homogeneous nucleation losses following the first evaporation tube furnace.

Similar to Karlsson et al. [35], they used a DMA to study the growth of Ag on SiO_2 and TiO_2 core particles.

Apart from homogeneous nucleation of shell material, another issue with using tube furnaces for evaporating a shell onto core aerosol NPs is that the entire aerosol undergoes the heating process, which can lead to evaporation of the core particles themselves and alloying between core and shell materials. An alternative PVD design, suggested and implemented in this work, is evaporation of a shell material by a local heater to avoid heating the entire aerosol to the same temperature as the evaporating material. The core aerosol is introduced to the PVD chamber through inlets and mixed with the shell material vapor to accomplish growth of a shell material, as shown in Fig. 2.4.

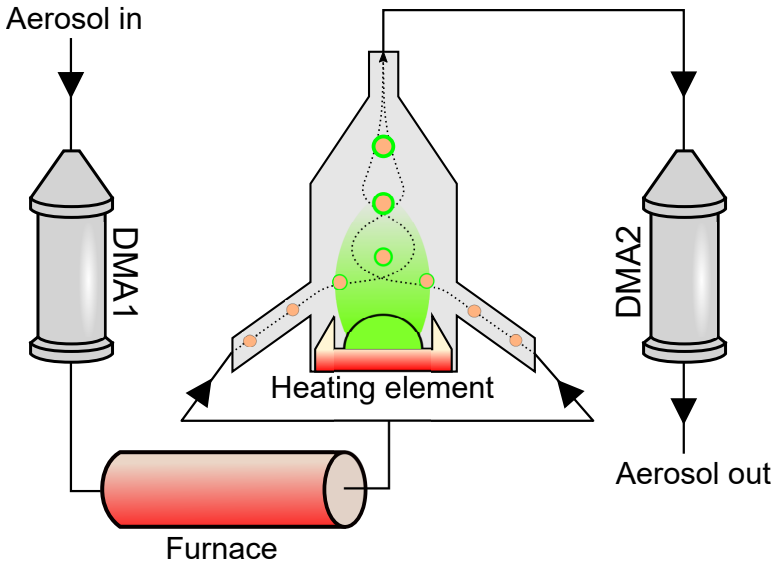

Figure 2.4: Schematic evaporator setup.

Positioning the evaporator after DMA1 and the tube furnace allows for deposition of a shell material onto compacted, monodisperse core particles. Scanning DMA2 allows us to study the growth as a shift in the electrical mobility size distribution toward larger electrical mobility diameters, shown in Fig. 2.5.

Zn is a convenient material to study in PVD growth due to its high evaporation rate at low temperatures, compared to other metals (Fig. 2.3). Growth by PVD is evident from the inset in Fig. 2.5, displaying a clear

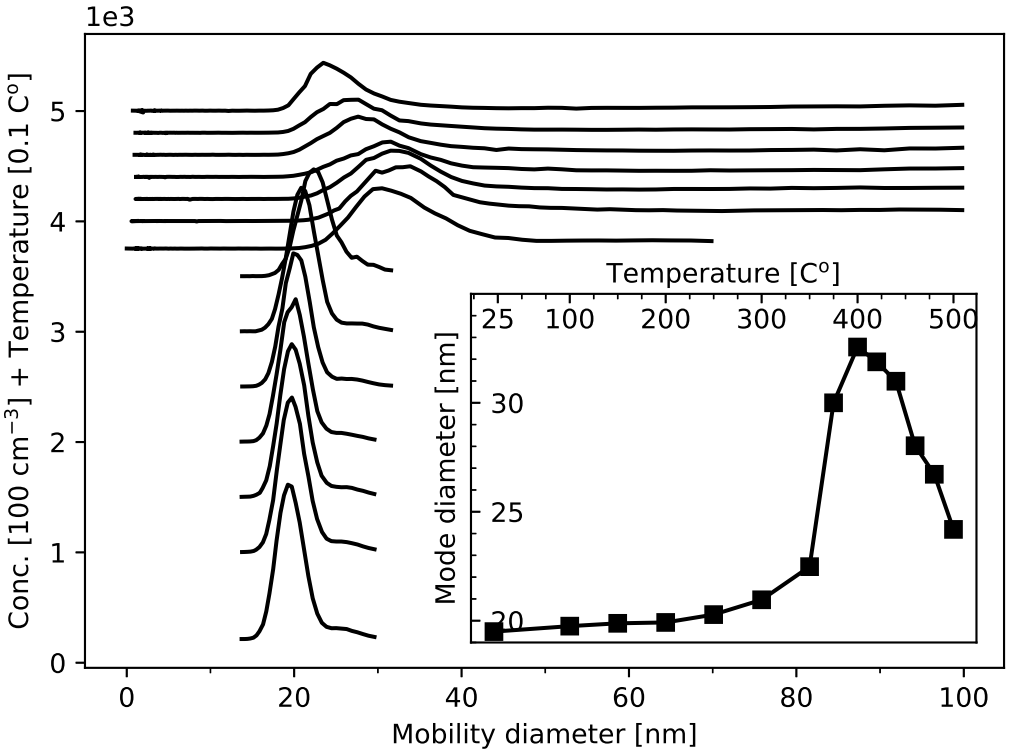

Figure 2.5: DMA scans of Zn growth onto Au core NPs. Note that the y-scale is a combination of concentration and evaporator temperature for appropriate spacing between each trace. Inset shows the shift in mean diameter, determined by Gaussian fits to each DMA scan, as function of evaporator temperature.

increase in the mean diameter of the DMA scans for increasing evaporator temperatures. The growth increases up to about 400 °C, after which growth decreases. This is likely due to a competing effect of self nucleation of Zn vapor in the supersaturated gas flow, similarly observed by Ref. [35], resulting in a leeching of Zn vapor. Note that the apparent lack of a Zn particle peak at small mobility diameters in the DMA traces in Fig. 2.5 is likely due to the absence of charges on these particles, being effectively invisible to the electrometer.

The sectional tube furnace approached by Harra et al. [36] to minimize self-nucleation of condensing Ag could lead to increased risk of alloying between the constituent elements. Ultimately, self-nucleation limits the PVD process in this setup. As discussed in Sec. 2.2.4, because growth rate is essentially independent of core particle diameter, homogenous nucleation may set an

upper limit for the shell thickness. Further, the thermal gradient in the chamber leads to loss of aerosol NPs by thermophoretic deposition, i.e. momentum transfer from hot gas to cold gas, effectively pushing aerosol NPs to deposit on sidewalls.

2.2.4 Modelling condensational shell growth

The rate of change of aerosol NP diameter in a PVD process can be described with kinetic gas theory (see Appendix A) from the rate of collisions between gaseous shell atoms and the aerosol NPs:

$$\frac{dd_p}{dt} = \frac{2M\alpha_C(p_v - p_d)}{\rho N_A\sqrt{2\pi mkT}} \tag{2.3}$$

where M, ρ, m and p_v is the molecular weight, density, mass and vapor pressure of the condensing species, N_A is Avogrado's constant, k is Boltzmann's constant and α_C is an accommodation factor (sticking probability), often taken to be unity. p_d, the increased vapor pressure over the curved particle surface, is expressed with the Kelvin equation:

$$p_d = p_s \exp\left(\frac{4\gamma M}{\rho RTd_p}\right) \tag{2.4}$$

where p_s is the equilibrium vapor pressure over a flat surface, γ is the surface energy of the particle and R is the gas constant. Eq. 2.4 states that the vapor pressure over NPs increases exponentially with decreasing diameter; it further implies that a supersaturation of the condensing vapor is required for net growth in Eq. 2.3. Interestingly, if we can neglect the Kelvin effect, eq. 2.3 states that the growth rate is diameter independent, a good approximation if the particle temperature is significantly lower than the evaporation temperature. This is shown in Fig. 2.6 for a simulated distribution of Au aerosol NPs growing at different Zn evaporation temperatures, with a lower, fixed aerosol NP temperature.

In reality, the particle temperature inside the evaporation chamber varies with position and evaporator temperature. Since this is difficult to measure, we have used Comsol Multiphysics to simulate an average time-temperature history for a group of particles travelling through a model of the chamber, at different evaporator temperatures. This allows for a more realistic view of Zn condensation/evaporation from the Au particles using the condensational

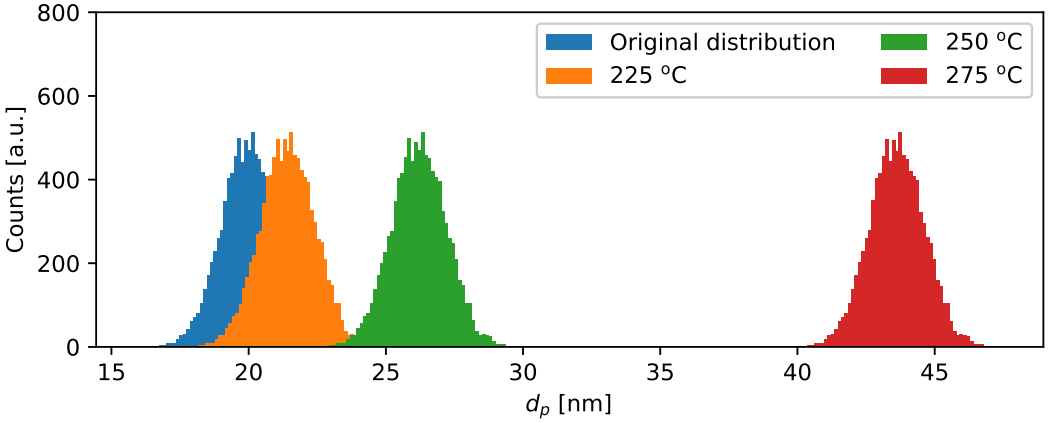

Figure 2.6: 10^4 $N(20\,\text{nm}, 1\,\text{nm})$ distributed Au aerosol NPs growing for 1.0 s at different Zn evaporation temperatures. The particle temperatures are assumed to be 100 °C in all cases, and the Zn vapor pressure is assumed constant throughout the growth.

growth equation (eq. 2.3), shown in top of Fig. 2.7. Using this time-temperature history, we can compare the growth expected by eq. 2.3 to the growth measured by the DMA setup, shown in the inset in Fig. 2.5.

Even at higher evaporator temperatures, the top plot in Fig. 2.7 shows that the particles experience only moderate temperatures during growth, making Zn re-evaporation from the Au core NPs negligible. Despite this, the observed growth deviates significantly from the theoretical final particle sizes in the bottom of Fig. 2.7. One reason for is that the constant Zn vapor pressure assumed throughout the growth process is a poor simplification; Zn vapor will quickly be lost to sidewalls (thermophoresis and diffusion) and homogenous nucleation, due to the high supersaturation and thermal gradient.

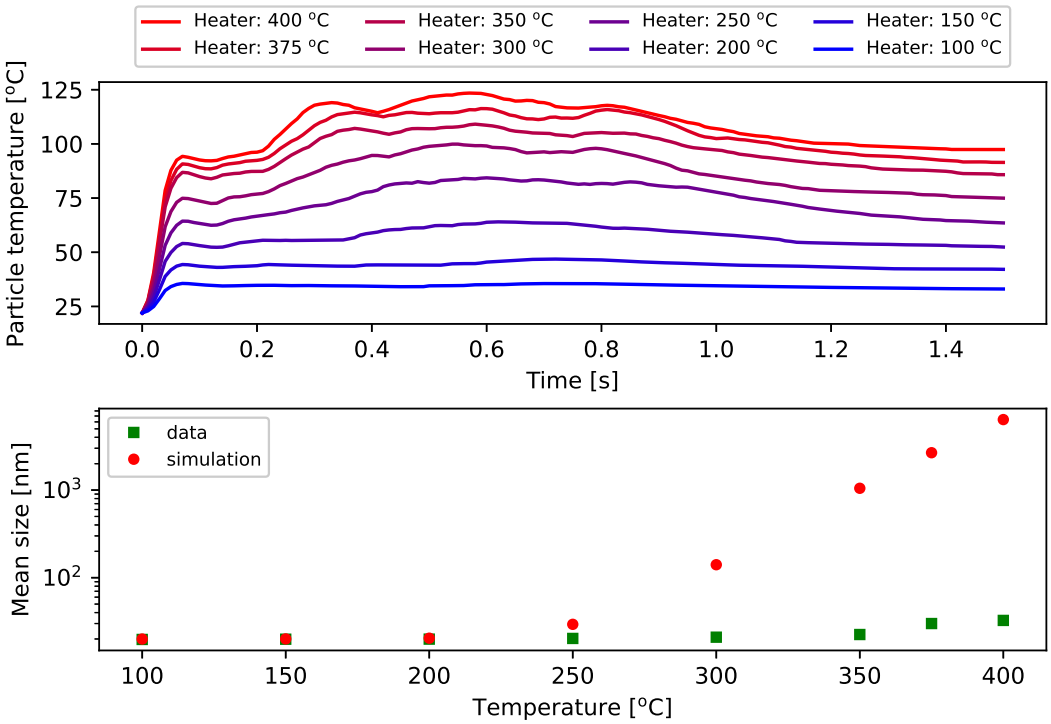

Figure 2.7: Top: particle time-temperature history in the evaporator by Comsol simulations. Bottom: measured and predicted growth of Zn on 20 nm Au aerosol NPs as function of evaporation temperature.

Ex situ characterization

3.1 Electron microscopy

Electron microscopy (EM) is an essential characterization technique for nanostructures, and superior to visible light microscopy in terms of resolution. Still, EM shares principal commonalities with light microscopes. In EM, the "light" source is an electron gun emitting electrons that are accelerated with an acceleration voltage V_{acc}, decreasing the electrons' de Broglie wavelengths to the order of picometers. The electron beam is manipulated with electromagnetic coil lenses and shaped to a broad beam or a small spot depending on imaging mode.

Upon interacting with the sample, the electron beam generates several signals that can be used to acquire different types of sample information and images. Two types of EM have been used here: scanning electron microscopy (SEM) and transmission electron microscopy (TEM). An SEM scans a converged electron beam and images the sample using electrons from the beam that reflect on the sample, called backscattered electrons (BSE), and/or electrons emitted from the sample, called secondary electrons (SE). SEM is a quick way to get an overview of size and shape of NPs, as well for measuring particle size distributions. Fig. 3.1 shows example SEM micrographs of aerosol NPs deposited with the ESP and the excellent monodispersity obtained when using the tandem DMA setup to size select the particles.

In a TEM, the electron beam is transmitted through the sample. Depending on the sample composition, and what angle from the optical axis the transmitted electrons are captured, we can get different image contrasts. The resolution is so high, that single atomic columns can be resolved. TEM is hence a unique technique to study the atomic structure of NPs. Many TEMs have the possibility to either image the sample with a parallel beam, conventional TEM (CTEM), or scanning a focused probe of the beam, called scanning TEM (STEM). Collecting electrons scattered at high angles, called high angle annular dark-field (HAADF) STEM, is excellent for multielemental structures, as the HAADF mass contrast scales with the atomic number as $\sim Z^{1.8}$. Fig. 3.2 shows an example of HAADF-STEM micrographs of 30 nm CuAg nanoparticles synthesized at different tube furnace temperatures. Mass contrast between Cu and Ag is clear at 750 °C and 950 °C, where we observe a quasi-Janus and core-shell morphology respectively.

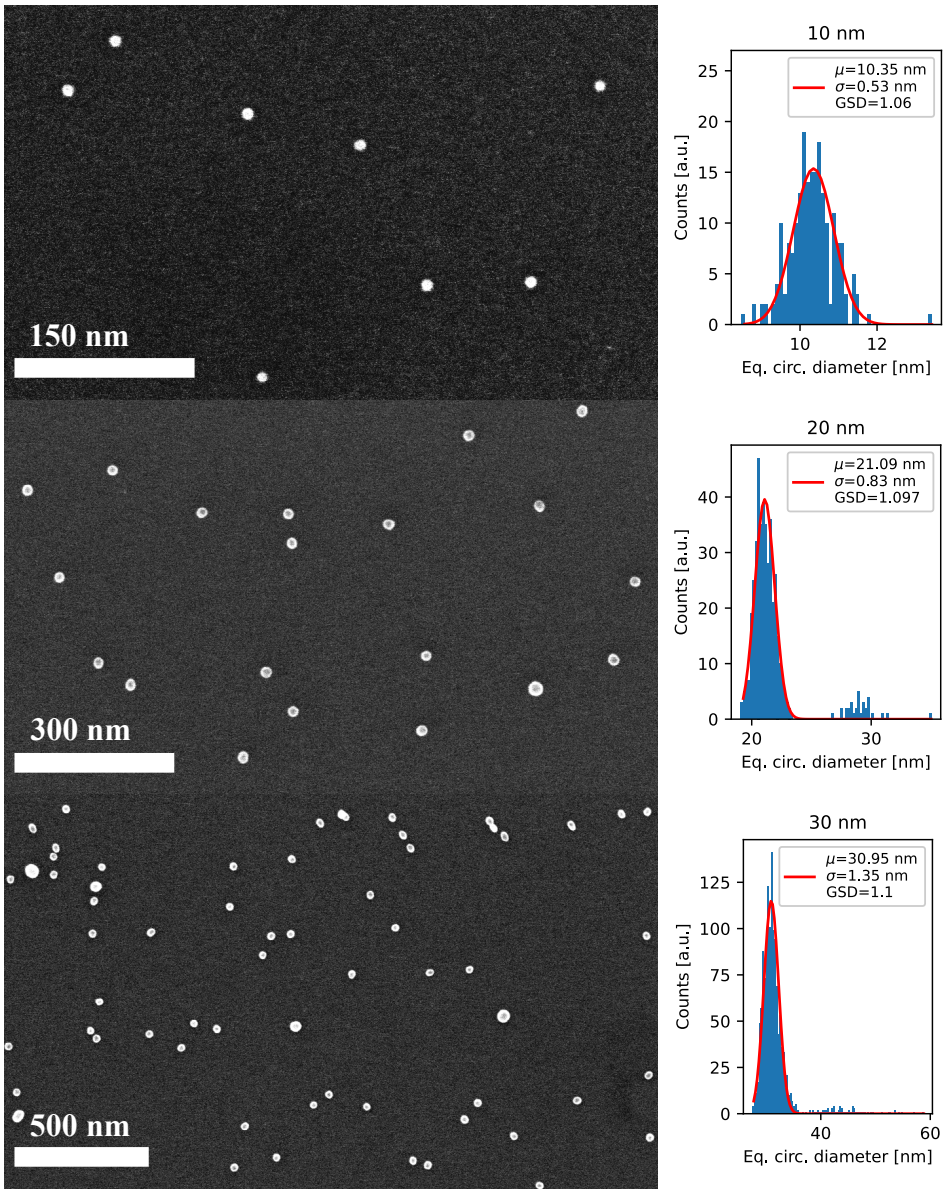

Figure 3.1: SEM micrographs (left column) and size distributions (right column) of tandem DMA size-selected CuAg particles deposited by ESP at electrical mobility set to 10 nm, 20 nm and 30 nm.

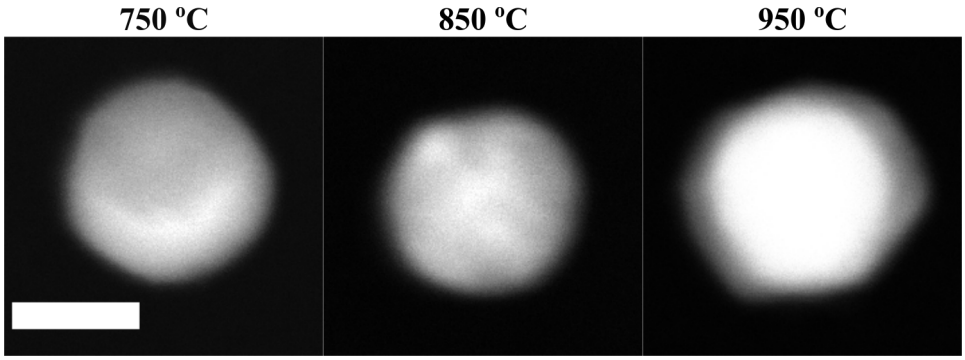

Figure 3.2: HAADF-STEM micrographs of ca. 30 nm CuAg aerosol nanoparticles compacted at furnace temperatures of 750 °C, 850 °C and 950 °C. Scale bar is 20 nm.

3.2 Energy dispersive X-ray spectroscopy

Irradiating a sample with an energetic electron beam will lead to some inelastic electron-electron collisions where the accelerated electrons can knock out a core electron in the sample. One way the excited atom can relax is recombining the core hole with an electron from a higher energy shell, emitting the energy difference as an element characteristic X-ray. These characteristic X-rays can be detected and analyzed with a technique called energy-dispersive X-ray spectroscopy (EDX).

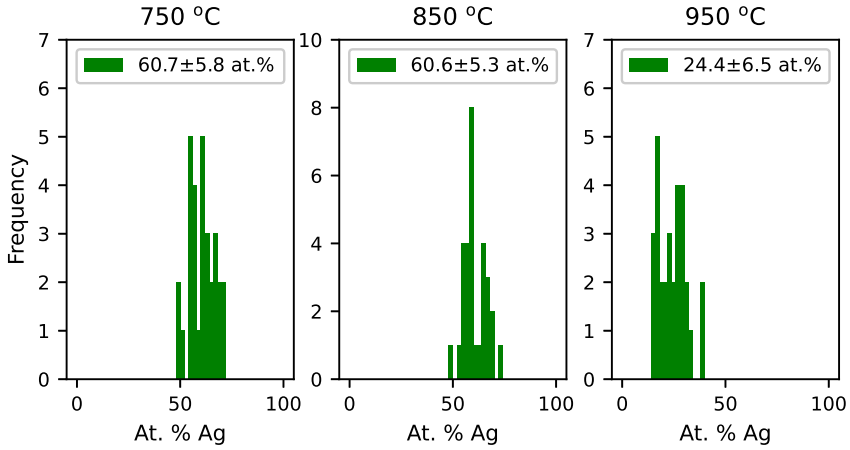

Figure 3.3: Ag distribution in CuAg aerosol particles synthesized at 750 °C, 850 °C and 950 °C.

Coupled with EM, we can image the sample *and* interrogate its elemental composition. Benefits of SEM-EDX is that we can obtain an ensemble-average of the sample composition by integrating the signal over a large number of particles. In (S)TEM-EDX, we can limit the beam size to interrogate individual NPs and obtain an inter-particle compositional variance. Inter-particle compositional variance is poorly understood for NPs generated by SDG, and was studied for the CuAg aerosol NPs in order to determine how the composition varies from one NP to the next by studying 30 individual particles per compaction temperature (750 °C, 850 °C and 950 °C; Fig. 3.3).

Fig. 3.3 supports that the observed second mobility diameter drop in the compaction curve (Fig. 2.2) is likely due to Ag evaporation, as the Ag content in the NPs compacted at 950 °C is significantly less than in NPs compacted at the lower temperatures. To the best of our knowledge, literature on compositional variance in bimetallic NPs generated by coagulating particles is scarce. The results here indicate that the variance is rather low, implying that aerosol synthesis routes can produce well defined bimetallic NPs not only in terms of size (Fig. 3.1), but also in composition. Indeed, the compositional variance here is comparable to that in optimized chemical synthesis routes [38].

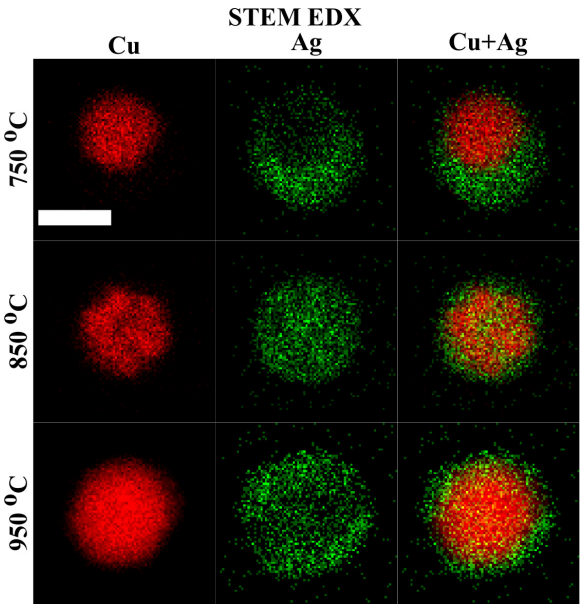

Figure 3.4: STEM-EDX maps of the CuAg particles in Fig. 3.2. Scale bar is 20 nm.

Further, using STEM-EDX with sub-nm probes, we can map the spatial extent of each element present in single NPs, arguably one of the most important techniques for core-shell NP characterization. In Fig. 3.4, STEM-EDX maps of the Cu-Ag particles in Fig. 3.2 show the elemental distribution of Cu and Ag, confirming a quasi-Janus morphology for particles synthesized at 750 °C and a core-shell morphology for particles synthesized at both 850 °C and 950 °C. For a definition of quasi-Janus NPs, see Sec. 3.4.

Studying the Au-Zn particles synthesized by on-line PVD as described in Sec. 2.2.3, STEM-EDX reveals that the particles did not adopt a core-shell morphology as expected, instead the elemental distribution suggest the NPs form an alloy phase (Fig 3.5).

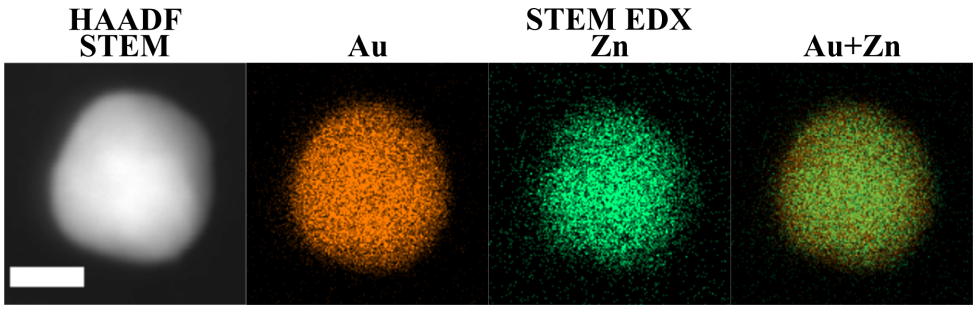

Figure 3.5: HAADF-STEM micrograph and STEM-EDX maps of AuZn particles generated by SDG and on-line PVD. Scalebar is 10 nm.

Since AuZn forms a variety of compounds over its compositional range, it is likely that the temperature-time history in the evaporator (Fig. 2.7) was significant enough to alloy the particles. This is a side-effect that is definitely present for miscible core-shell materials using PVD with a tube furnace where the entire aerosol is heated [35, 36] and seems unfortunately to be an issue with our design of a local heater, at least in the present chamber design with the settings used to synthesize the particles in Fig. 3.5. It is however questionable if a different chamber design where the core particle temperature is kept even lower would lead to the intended effect of adatom shell growth. Instead, a steeper thermal gradient may promote homogenous nucleation of the evaporating species, and hence growth of core particles via coagulation.

3.2.1 Unmixing EDX maps to quantify chemical phases

While EDX maps like the ones in Fig. 3.4 can lead to insight in terms of how elements distribute in multielemental NPs, EDX is inherently limited in that it only can yield elemental data. However, the data format of EDX maps lends itself well to be studied by "big data" multivariate statistical methods. The basic idea for these methods applied to EDX and similar techniques is to linearly decompose the spectra to *spectral components* and their corresponding *loadings* for each spatial position [39, p. 27]. The spectral components can in some cases be interpreted as *chemical* phases in the sample, with the spatial distribution of these phases given by the loadings. An impressive example on core-shell NPs is the analysis by Rossouw et al. [40], where the spectral components accurately described the core and shell compositions, as verified by analysing pure core and pure shell NPs separately.

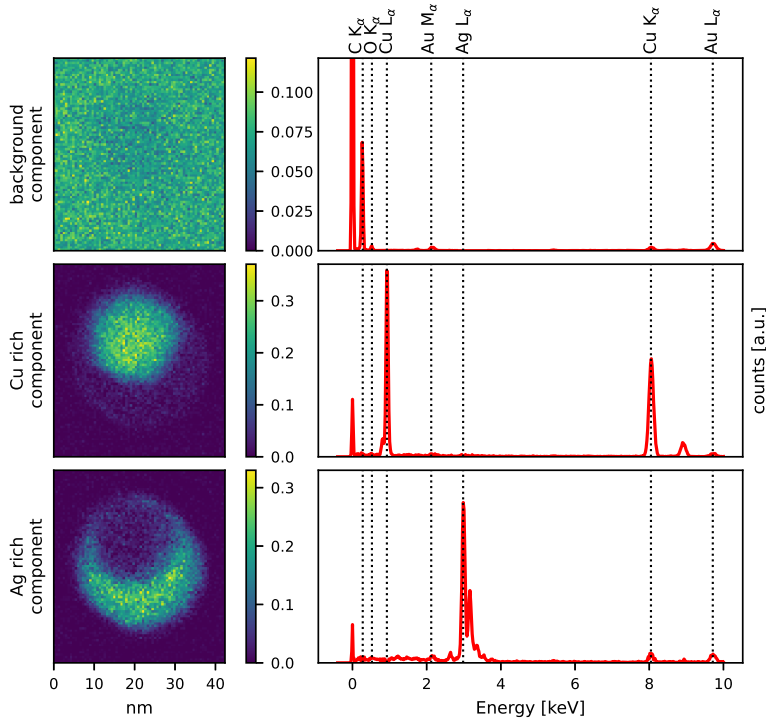

Figure 3.6: NMF of the STEM-EDX map of the core-shell CuAg NP compacted at 750 °C in Fig. 3.4, with spectral components in the right column and loading maps in the left column.

For hyperspectral data such as EDX, principal component analysis (PCA) is the most common multivariate method. In PCA, a dataset with a large number of correlated variables (here: energy channels) is reduced to a small set of uncorrelated variables, representing new spectral components of the dataset; their weight in each observation (pixel) is the loadings [39, p. 28]. EDX maps can be thought of as a data cube with dimensions $i \times j$ number of pixels (observations), times k number of channels (variables), typically 1024 to 2048. PCA, then, takes the k channels and reduces them to $n < k$ spectral components consisting of a linear, uncorrelated mix of the k original channels. The spatial distribution of these can then be represented in new maps of the spectral component maps, where each spectral component in some cases can be related to chemical phases of the sample [39].

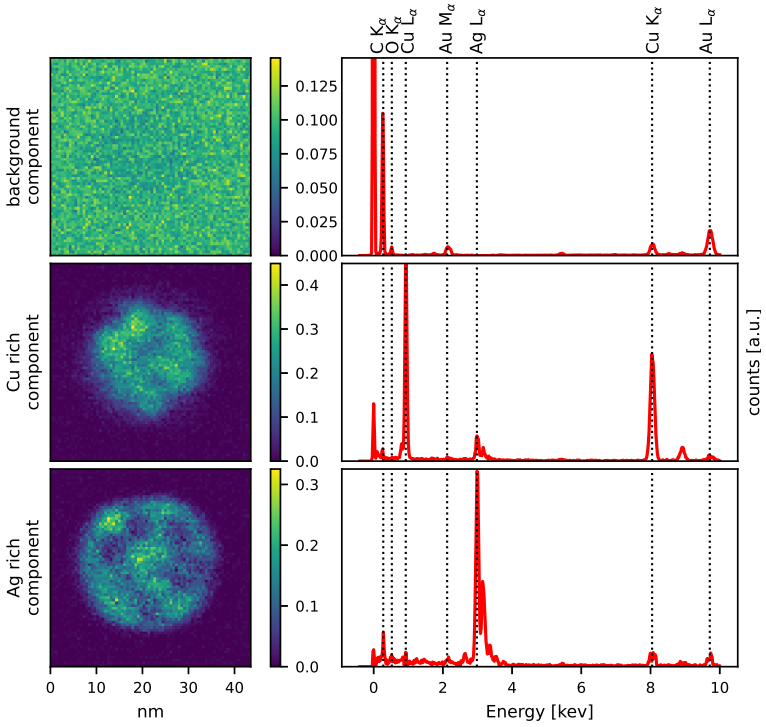

Figure 3.7: NMF of the STEM-EDX map of the core-shell CuAg NP compacted at 850 °C in Fig. 3.4, with spectral components in the right column and loading maps in the left column.

One issue with PCA is the orthogonality restriction on the new spectral components; they can, for instance, contain negative intensities, which lim-

its physical interpretation. To overcome this, a related technique called non-negative matrix factorization (NMF) has been used in this work to decompose EDX maps. NMF is similar to PCA, except it puts additional constraints on the new spectral components such that they cannot be negative. This is a natural constraint on spectral data since we would in reality not record negative intensities [39, p. 34]. The result of performing NMF on the STEM-EDX maps in Fig. 3.4 is shown in Figs. 3.6 – 3.8.

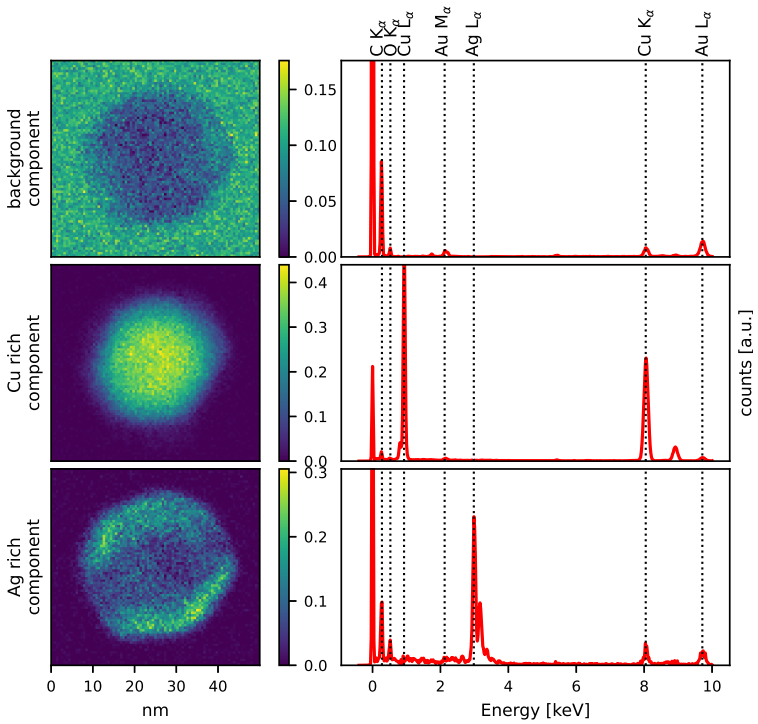

Figure 3.8: NMF of the STEM-EDX map of the core-shell CuAg NP compacted at 950 °C in Fig. 3.4, with spectral components in the right column and loading maps in the left column.

Figs. 3.6 – 3.8 display the ability of NMF to unmix Cu rich and Ag rich parts. For the quasi-Janus particle (Fig. 3.6), a Cu face is separated from an Ag face; for the core-shell particles in Figs. 3.7 and 3.8, we see a Cu rich core separated from an Ag rich shell. In contrast to the EDX-maps in Fig. 3.4, the core and shell parts are characterized by different spectral components that can be separately quantified. Hence, we can estimate the chemical composition of the core and shell separately, summarized in table

3.1.

The ability to separate overlapping phases in complex nanostructures such as these particles makes NMF superior to other multivariate techniques like clustering. One must however carefully note that strongly overlapping phases, like those in the core-shell NPs, may be susceptible to some signal-mixing. For instance, Cu and Ag signal from the core may show up in the shell and vice versa. The extent of this problem may be larger for NPs with more intermixed phases (i.e. particles compacted at 850 °C; Fig. 3.7) compared to NPs with more separated phases (i.e. particles compacted at 750 °C and 950 °C; Figs. 3.6 and 3.8).

Table 3.1: Average composition in Cu rich and Ag rich spectral components determined by NMF.

	750 °C		850 °C		950 °C	
	Cu-rich phase	Ag-rich phase	Cu core	Ag shell	Cu core	Ag shell
Cu (at. %)	97.9 ± 3.0	11.7 ± 2.2	89.4 ± 3.5	11.8 ± 1.5	99.9 ± 0.1	28.0 ± 8.1
Ag (at. %)	2.1 ± 3.0	88.3 ± 2.2	10.6 ± 3.5	88.2 ± 1.5	0.1 ± 0.1	72.0 ± 8.1

3.3 X-ray photo-electron spectroscopy

Illuminating NP samples with X-rays can, like the electron beam, eject core electrons from sample atoms. These electrons can be captured and analyzed using X-ray photo-electron spectroscopy (XPS). Unlike EDX, XPS can obtain compositional information and chemical state information by measuring the photo-electrons' kinetic energy: relating it with the photon energy, we obtain the electron binding energy which will be a function of the bonding environment of the atom ejecting the photo-electron. XPS can therefore complement EDX analysis, which only provides elemental information. On the other hand, XPS always provides an ensemble average of NP properties, and is very surface sensitive: photo-electrons can only penetrate through the first few atomic layers of the NPs, whereas characteristic X-rays come from the entire NP. Nonetheless, XPS is valuable when characterizing core-shell NP surfaces.

Figs. 3.9 and 3.10 show Cu and Ag XPS spectra obtained at MAX IV for 30 nm CuAg particles compacted at 850 °C (Fig. 3.4), normalized by beam intensity and photo-absorption cross sections. Asymmetric Doniach-Sunjic lines were fitted to the main peaks and integrated to estimate the relative surface concentrations of Cu and Ag, shown in Table 3.2.

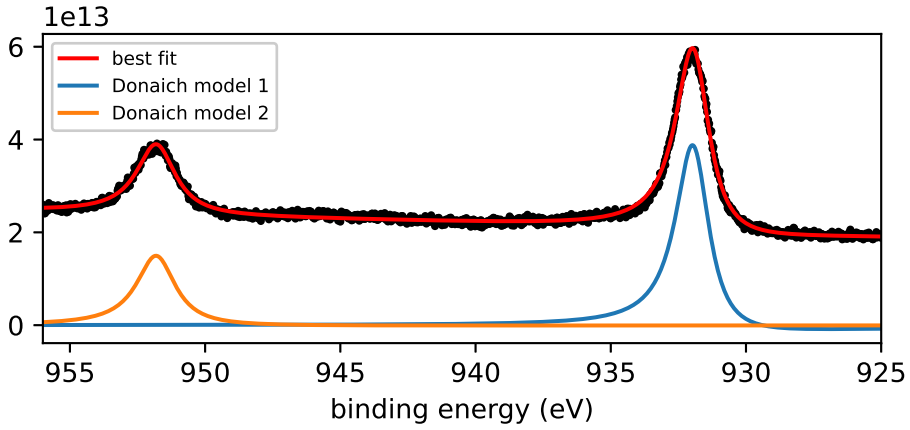

Figure 3.9: Cu 2p 3/2 and 1/2 XPS spectra.

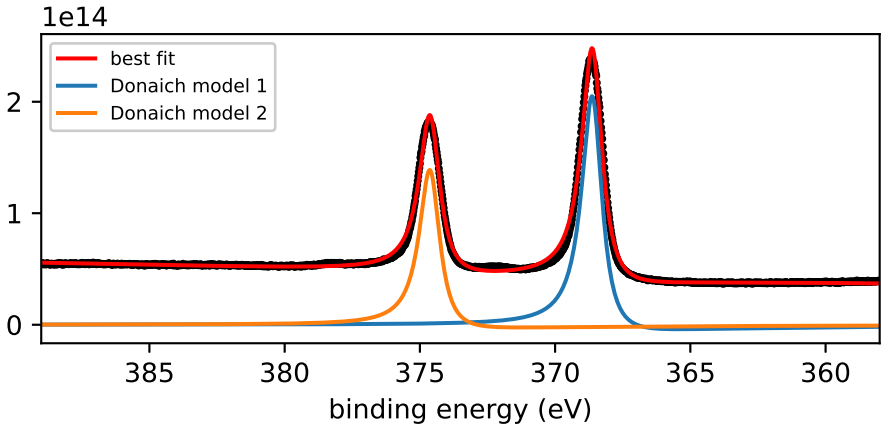

Figure 3.10: Ag 3d 5/2 and 3/2 XPS spectra.

Table 3.2: Surface composition of 30 nm Cu-Ag NPs compacted at 850 °C, determined by XPS.

	Cu (at.%)	Ag (at.%)
Shell composition	22	78

Compared to the shell composition obtained by NMF for particles synthesized in identical conditions (Table 3.1), the XPS quantification results in

Table 3.2 agree quite well. The slightly higher Cu concentration obtained by XPS could be due to sample ageing leading to minor Cu oxidation and a higher presence of Cu at NP surfaces. This is however challenging to verify with the current spectral information in Fig. 3.9 as Cu and Cu^+ have very similar spectral features.

Combining XPS analysis as an independent surface sensitive technique with multivariate analysis of EDX maps is an important step to verify the validity of machine learning methods like NMF for chemical quantification, and something that to the best of our knowledge has not been considered before.

3.4 Surface segregation

The preceding sections 3.1 – 3.3 have demonstrated the feasibility to synthesize aerosol core-shell Cu-Ag NPs without a separate coating step like that used in PVD. The reason for this result is attributed to surface segregation, where one element segregates toward the surface of the particle. In this setup, the thermal treatment in the tube furnace (Fig. 2.1) is the driving force that enables Ag to enrich at the surface as demonstrated in Figs. 3.4 – 3.8.

Producing core-shell NPs via this route requires tinkering in the choice of materials. Firstly, the constituents should have low solubility, which indeed is the case for Cu and Ag. Why is Ag preferred at the surface? A general observation in immiscible NP systems is that the element with the larger atomic radius and lower surface energy tends to occupy the surface [41]. This, too, is the case for the Cu-Ag system (see Paper I).

As the Cu-Ag aggregates pass through the tube furnace, the thermal energy allow them to compact (Fig. 2.2); at higher temperatures, surface segregation occurs to create well-defined Cu and Ag domains in the particles. At lower temperatures (750 °C), the particles obtain a quasi-Janus morphology, shown in Figs. 3.4 and 3.6. Janus, named after the two-faced Roman god, indicates the presence of a Cu and Ag face. Quasi-Janus here means that the particles are not exactly divided in two "faces", rather Ag wraps around the Cu face, most clearly seen in Fig. 3.6.

Similar observations for the Cu-Ag system have been made for synthesis by surface dewetting [42] and chemical synthesis [43]. In the former work, the authors attributed the substrate temperature and Ag content being deciding factors for the Janus or core-shell morphology, where a higher Ag content

lead to a prevalence of the Janus morphology. More specifically, the authors identified a critical Ag shell thickness of 3 nm to 4 nm, beyond which the Janus configuration was preferred. Assuming a "perfect" core-shell morphology (see definition in Appendix B) for particles in the STEM-EDX maps (Fig. 3.4) with the average composition determined by TEM-EDX in Fig. 3.3, a simple geometrical derivation (eq. B.3 in Appendix B) leads to shell thickness estimations of ca. 4.9 nm, 4.8 nm and 1.8 nm, for the CuAg NPs compacted at 750 °C, 850 °C and 950 °C, respectively. Though the shell thicknesses are not exactly comparable due to core-shell mixing as determined by NMF (Table 3.1), a high Ag content can in aerosol NPs can lead to both quasi-Janus and core-shell morphologies, depending on compaction temperatures.

Interestingly, in the chemical synthesis approach, the authors in Ref. [43] determine the opposite trend; that is, a higher Ag content lead to a transition from a quasi-Janus morphology to a core-shell morphology, in contrast to what was observed in the thermal dewetting synthesis by Ref. [42]. In their thermodynamical model, the energy difference between the quasi-Janus and core-shell configurations decrease with increasing Ag content, such that the core-shell morphology may prevail for high Ag contents.

In contrast to both methods presented by Refs. [42, 43], we observe a core-shell configuration for low *and* high Ag contents in compacted aerosol NPs. The stability of the core-shell NPs compacted at 850 °C which had a significantly higher Ag content than the ones compacted at 950 °C may benefit from the increased solubility of Ag in Cu, and Cu in Ag (Table 3.1). Indeed, the higher compaction temperature at 950 °C may promote Ag surface segregation, albeit the cost of Ag evaporation that simultaneously leads to the formation of a thinner shell. It is interesting to note that we can tune the chemical configuration mainly through the compaction temperature (through evaporation), although recent work on SDG process control indicates composition can be tuned directly in the synthesis step by changing certain process parameters [44]. Compared to other physical and chemical routes, the aerosol synthesis with an equilibrating heat treatment allow us to study surface segregation in unsupported NPs, free from influence by supporting substrate and chemicals.

In our recently published paper (Paper I), we compared molecular dynamics (MD) simulations of the Cu-Ag system to our experimental findings. Using the embedded-atom potential by Ref. [45], we were able to closely replicate the experimental findings (Fig. 3.4) by using the same chemical composition

determined by TEM-EDX (Fig. 3.3) and compaction temperatures used in the synthesis. Although MD simulations cannot afford a system of the same size as our 30 nm particles, a similar trend of transition from quasi-Janus to core-shell was observed for smaller (2.5 nm to 4.2 nm) and larger (ca. 10 nm) particles alike, simply by increasing the compaction temperature.

Conclusion and outlooks

Aerosol synthesis is a promising route to synthesize core-shell NPs. In this work, we have studied two fundamentally different aerosol processes to obtain core-shell particles: PVD by thermal evaporation and heat-induced surface segregation. Instead of the previously studied approaches to connect additional tube furnaces for evaporation, we have to a high extent decoupled the heating of shell material and the aerosol by a newly designed PVD reactor in which material is locally heated and evaporated. While simulations indicated the aerosol can be kept at a significantly lower temperature than the evaporator, it was high enough to alloy the core Au aerosol NPs and the condensing Zn. The high thermal gradient further limits the shell growth process due to homogenous nucleation and thermophoresis of the gaseous Zn.

Still, PVD with local heating could be a more appropriate and preferable design choice than evaporation with a tube furnace. To study the growth process better, switching core and shell materials to an immiscible combination is a rational step forward. Precisely this approach was used to successfully demonstrate aerosol synthesis of quasi-Janus and core-shell particles by heat-induced surface segregation of Cu and Ag. Machine learning algorithms on STEM-EDX maps allowed us to determine the composition of chemical phases of the core and shell components, the accuracy of which was compared to XPS as an independent surface composition technique. Investigating applicability and accuracy of chemical phase composition determination by multivariate methods like NMF is a worthwhile endeavour, especially for core-shell nanoparticles, as it may extend the fundamental capabilities of EDX beyond elemental spectroscopy. For that reason, it is a logic strategy to compare results obtained by NMF to other compositional techniques like XPS, as well as modelling. The abilities and limitations of algorithms like NMF to separate between strongly overlapping and/or intermixing phases, as in the Cu-Ag core-shell NPs compacted at 850 °C, is another open question that requires further attention.

Currently, other material systems suitable for core-shell synthesis by surface segregation are being studied in our group using Molecular Dynamics simulations [46], and a continued research route will be to compare these systems experimentally. To that end, the aerosol route may be ideal to study this phenomenon as the particles are unsupported by substrates and solvents. To

ensure a desired morphology, controlling the chemical composition may be key, yet studying the compositional homogeneity is often overlooked in gas phase synthesis of NPs. For that reason, we carefully considered the inter-particle compositional variance by interrogating 30 individual CuAg NPs with TEM-EDX. It was found that the compositional variance was low – comparable to optimized chemical methods [38] – which is a further benefit of SDG as a NP synthesis method. The reason for the narrow compositional distribution in spark ablation is unknown and remain to be explored. Additionally, controlling the discharge process in spark ablation has demonstrated the feasibility of tuning the NP composition by changing the circuit resistance [44]. We have made similar investigations and this will be further studied within this project.

Bibliography

[1] R. Ghosh Chaudhuri and S. Paria. "Core/shell nanoparticles: classes, properties, synthesis mechanisms, characterization, and applications". In: *Chemical reviews* 112.4 (2011), pp. 2373–2433.

[2] P. Mélinon et al. "Engineered inorganic core/shell nanoparticles". In: *Physics Reports* 543.3 (2014), pp. 163–197.

[3] M. Haruta. "Catalysis of gold nanoparticles deposited on metal oxides". In: *Cattech* 6.3 (2002), pp. 102–115.

[4] M. V. Yezhelyev et al. "Emerging use of nanoparticles in diagnosis and treatment of breast cancer". In: *The lancet oncology* 7.8 (2006), pp. 657–667.

[5] W. Liu et al. "Colloidal InSb Nanocrystals". In: *Journal of the American Chemical Society* 134.50 (2012), pp. 20258–20261.

[6] W. Hinds. *Aerosol Technology Properties, Behavior, and Measurement of Airborne Particles Second Edition*. 2012.

[7] M. H. Magnusson et al. "Gold nanoparticles: production, reshaping, and thermal charging". In: *Journal of Nanoparticle Research* 1.2 (1999), pp. 243–251.

[8] R. T. Hallberg et al. "Hydrogen-assisted spark discharge generated metal nanoparticles to prevent oxide formation". In: *Aerosol Science and Technology* 52.3 (2018), pp. 347–358.

[9] L. A. Bahr et al. "In situ analysis of aerosols by Raman spectroscopy–Crystalline particle polymorphism and gas-phase temperature". In: *Journal of Aerosol Science* 126 (2018), pp. 143–151.

[10] T. V. Pfeiffer et al. "Precursor-less coating of nanoparticles in the gas phase". In: *Materials* 8.3 (2015), pp. 1027–1042.

[11] M. A. Hines and P. Guyot-Sionnest. "Synthesis and characterization of strongly luminescing ZnS-capped CdSe nanocrystals". In: *The Journal of Physical Chemistry* 100.2 (1996), pp. 468–471.

[12] C. G. Hadjipanayis et al. “Metallic iron nanoparticles for MRI contrast enhancement and local hyperthermia”. In: *Small* 4.11 (2008), pp. 1925–1929.

[13] S. Gong, Y.-X. Zhang, and Z. Niu. “Recent Advances in Earth-Abundant Core/Noble-Metal Shell Nanoparticles for Electrocatalysis”. In: *ACS Catalysis* 10.19 (2020), pp. 10886–10904.

[14] P. Solař et al. “Composite Ni@ Ti nanoparticles produced in arrow-shaped gas aggregation source”. In: *Journal of Physics D: Applied Physics* 53.19 (2020), p. 195303.

[15] D. Llamosa et al. “The ultimate step towards a tailored engineering of core@ shell and core@ shell@ shell nanoparticles”. In: *Nanoscale* 6.22 (2014), pp. 13483–13486.

[16] S. Schwyn, E. Garwin, and A. Schmidt-Ott. “Aerosol generation by spark discharge”. In: *Journal of Aerosol Science* 19.5 (1988), pp. 639–642.

[17] J. Feng, G. Biskos, and A. Schmidt-Ott. “Toward industrial scale synthesis of ultrapure singlet nanoparticles with controllable sizes in a continuous gas-phase process”. In: *Scientific reports* 5.1 (2015), pp. 1–9.

[18] R. Reinmann and M. Akram. “Temporal investigation of a fast spark discharge in chemically inert gases”. In: *Journal of Physics D: Applied Physics* 30.7 (1997), pp. 1125–1134. DOI: 10.1088/0022-3727/30/7/010. URL: https://doi.org/10.1088/0022-3727/30/7/010.

[19] N. S. Tabrizi et al. “Generation of nanoparticles by spark discharge”. In: *Journal of Nanoparticle Research* 11.2 (2009), p. 315.

[20] J. Borra et al. “Electrical discharge regimes and aerosol production in point-to-plane DC high-pressure cold plasmas: aerosol production by electrical discharges”. In: *Journal of aerosol science* 29.5-6 (1998), pp. 661–674.

[21] J. H. Byeon, J. H. Park, and J. Hwang. “Spark generation of monometallic and bimetallic aerosol nanoparticles”. In: *Journal of Aerosol Science* 39.10 (2008), pp. 888–896.

[22] K. E. Lehtinen and M. R. Zachariah. “Energy accumulation in nanoparticle collision and coalescence processes”. In: *Journal of Aerosol Science* 33.2 (2002), pp. 357–368.

[23] J. Feng et al. “General approach to the evolution of singlet nanoparticles from a rapidly quenched point source”. In: *The Journal of Physical Chemistry C* 120.1 (2016), pp. 621–630.

[24] N. Tabrizi et al. “Generation of mixed metallic nanoparticles from immiscible metals by spark discharge”. In: *Journal of Nanoparticle Research* 12.1 (2010), pp. 247–259.
[25] V. A. Vons et al. “Silicon nanoparticles produced by spark discharge”. In: *Journal of Nanoparticle Research* 13.10 (2011), pp. 4867–4879.
[26] S. Kala, R. Theissmann, and F. E. Kruis. “Generation of AuGe nanocomposites by co-sparking technique and their photoluminescence properties”. In: *Journal of nanoparticle research* 15.9 (2013), pp. 1–12.
[27] M. E. Messing et al. “Generation of Pd model catalyst nanoparticles by spark discharge”. In: *The Journal of Physical Chemistry C* 114.20 (2010), pp. 9257–9263.
[28] M. Karlsson. “Methods to Generate Size-and Composition Controlled Aerosol Nanoparticles”. PhD thesis. 2004.
[29] C. Preger. “Magnetic-field-directed Self-assembly of Multifunctional Aerosol Nanoparticles”. PhD thesis. 2020.
[30] J. Dixkens and H. Fissan. “Development of an electrostatic precipitator for off-line particle analysis”. In: *Aerosol Science & Technology* 30.5 (1999), pp. 438–453.
[31] C. Preger et al. “Predicting the deposition spot radius and the nanoparticle concentration distribution in an electrostatic precipitator”. In: *Aerosol Science and Technology* 54.6 (2020), pp. 718–728.
[32] M. Messing. “Engineered Nanoparticles Generation, Characterization and Applications”. PhD thesis. 2011.
[33] M. Karlsson et al. “Compaction of agglomerates of aerosol nanoparticles: A compilation of experimental data”. In: *Journal of Nanoparticle Research* 7.1 (2005), pp. 43–49.
[34] C. Alcock, V. Itkin, and M. Horrigan. “Vapour pressure equations for the metallic elements: 298–2500K”. In: *Canadian Metallurgical Quarterly* 23.3 (1984), pp. 309–313.
[35] M. N. Karlsson et al. “Size-and composition-controlled Au–Ga aerosol nanoparticles”. In: *Aerosol science and technology* 38.9 (2004), pp. 948–954.
[36] J. Harra et al. “Coating of silica and titania aerosol nanoparticles by silver vapor condensation”. In: *Aerosol Science and Technology* 49.9 (2015), pp. 767–776.
[37] A. M. Boies et al. “Gas-phase production of gold-decorated silica nanoparticles”. In: *Nanotechnology* 22.31 (2011), p. 315603.
[38] C. Srivastava, D. E. Nikles, and G. B. Thompson. “Tailoring nucleation and growth conditions for narrow compositional distributions

in colloidal synthesized FePt nanoparticles". In: *Journal of Applied Physics* 104.10 (2008), p. 104314.

[39] P. T. Besa. "Development of novel EELS methods to unveil nanoparticle properties". PhD thesis. Universitat de Barcelona, 2019.

[40] D. Rossouw et al. "Multicomponent signal unmixing from nano heterostructures: Overcoming the traditional challenges of nanoscale X-ray analysis via machine learning". In: *Nano letters* 15.4 (2015), pp. 2716–2720.

[41] R. Ferrando, J. Jellinek, and R. L. Johnston. "Nanoalloys: from theory to applications of alloy clusters and nanoparticles". In: *Chemical reviews* 108.3 (2008), pp. 845–910.

[42] C. Langlois et al. "Transition from core–shell to Janus chemical configuration for bimetallic nanoparticles". In: *Nanoscale* 4.11 (2012), pp. 3381–3388.

[43] W. T. Osowiecki et al. "Tailoring morphology of Cu–Ag nanocrescents and core–shell nanocrystals guided by a thermodynamic model". In: *Journal of the American Chemical Society* 140.27 (2018), pp. 8569–8577.

[44] A. Kohut et al. "Full range tuning of the composition of Au/Ag binary nanoparticles by spark discharge generation". In: *Scientific reports* 11.1 (2021), pp. 1–10.

[45] P. Williams, Y. Mishin, and J. Hamilton. "An embedded-atom potential for the Cu–Ag system". In: *Modelling and Simulation in Materials Science and Engineering* 14.5 (2006), p. 817.

[46] N. Eom et al. "General Trends in Core–Shell Preferences for Bimetallic Nanoparticles". In: *ACS nano* (2021).

Appendix A
Condensational growth of aerosol nanoparticles

The rate at which an aerosol NP grows or shrinks due to condensation or evaporation, respectively, is nothing but the rate at which atoms from the gas arrive minus the rate at which atoms from the NP leave. Multiplying that with the atomic volume will yield the rate of volume change, which can be translated to the rate of diameter change of the aerosol NP, a convenient formulation when using DMAs to measure NP diameter.

To derive an expression for condensational growth of aerosol NPs, we need to know the rate at which atoms in the gas hit an aerosol NP of area A. We can analogously think of how many gas molecules that pass an area A in the same direction during Δt in one dimension (flux), #collisions/$\Delta t A$. In Δt, this will be

$$z = \langle v_x^+ \rangle \, n \tag{A.1}$$

where $\langle v_x^+ \rangle$ is the average 1D positive velocity and n is the concentration of gas molecules. In 1D, the Maxwell-Boltzmann distribution of gas molecule velocities is

$$f(v_x)\, dv_x = \sqrt{\frac{m}{2\pi kT}} e^{-mv_x^2/2kT}\, dv_x \tag{A.2}$$

We are interested in the average velocity of molecules travelling in positive x, given by

$$\langle v_x^+ \rangle = \int_0^\infty v_x \sqrt{\frac{m}{2\pi kT}} e^{-mv_x^2/2kT}\, dv_x = \sqrt{\frac{kT}{2\pi m}} \tag{A.3}$$

Putting it together, the number of collisions per area per time becomes

$$z = n\sqrt{\frac{kT}{2\pi m}} = \frac{p_v}{kT}\sqrt{\frac{kT}{2\pi m}} = \frac{p_v}{\sqrt{2\pi m kT}} \tag{A.4}$$

where we have used that the gas concentration n can be written as p_v/kT, where p_v is the vapor pressure of the gas, using the ideal gas law.

To obtain an expression for growth, we have to consider the net rate of arrival of gas molecules. The net rate of arrival is the rate of gas molecules

hitting the aerosol NP, z_{in}, minus the rate of gas molecules leaving the NP, z_{out}. The evaporation rate z_{out} is the same as eq. A.4, with p_v replaced by p_d, the vapor pressure of the condensing gas over the NP. It is customary to include a "sticking coefficient" α_C, that gives the probability of a condensing gas species to be retained on the particle. The net rate of arrival of gas molecues or atoms to the NP surface now becomes $n_z = (z_{in} - z_{out})A_p$, where $A_p = \pi d_p^2$ is the area of the aerosol NP of diameter d_p. Using eq. A.4, we get

$$n_z = \frac{\pi d_p^2 \alpha_C (p_v - p_d)}{\sqrt{2\pi m k T}} \tag{A.5}$$

Eq. A.5 can be translated to rate of NP volume change as

$$\frac{dv_p}{dt} = n_z v_m \tag{A.6}$$

where $v_m = M/\rho N_A$ is the condensing species' volume. Since $v_p = d_p^3 \pi/6$ we can write the change in NP diameter as

$$\frac{dv_p}{dt} = \underbrace{\frac{dv_p}{dd_p}}_{=\frac{d_p^2\pi}{2}} \frac{dd_p}{dt} \rightarrow \frac{dd_p}{dt} = \frac{2M\alpha_C(p_v - p_d)}{\rho N_A \sqrt{2\pi m k T}} \tag{A.7}$$

The vapor pressure p_v for a material at a temperature T is tabulated; p_d, the pressure over a spherical particle, is given by the Kelvin equation:

$$p_d = p_s \exp\left(\frac{4\gamma M}{\rho R T d}\right) \tag{A.8}$$

where p_s is the saturation vapor pressure, γ is the surface tension, M is the molecular weight. We see that evaporation is significant at higher temperatures and for NPs with small diameters d, leading to a slower rate of growth for smaller NPs. Note that for net growth, the actual vapor pressure p_v needs to be greater than the saturation vapor pressure p_s over the aerosol NP, else $p_d > p_v$ and the NP will shrink.

Appendix B
Shell thickness of ideal core-shell nanoparticles

Consider an ideal, perfectly spherical core-shell nanoparticle, where the spherical core is made of some material A and the shell of some material B. The volume of the core and shell are given by $V_{\text{core}} = \frac{4\pi}{3} r_{\text{core}}^3$ and $V_{\text{shell}} = \frac{4\pi}{3}(r_{\text{particle}} - r_{\text{core}})^3$, respectively. Hence, we have

$$n_A = \frac{V_{\text{core}}}{V_M^A} = \frac{\frac{4\pi}{3} r_{\text{core}}^3}{V_M^A}$$

moles of material A (core material) and

$$n_B = \frac{V_{\text{shell}}}{V_M^B} = \frac{\frac{4\pi}{3}(r_{\text{particle}}^3 - r_{\text{core}}^3)}{V_M^B}$$

moles of material B (shell material) in the core-shell nanoparticle, where V_M^A and V_M^B are the molar volumes of material A and B respectively. c_B can therefore be expressed as

$$c_B = \frac{n_B}{n_A + n_B} = \frac{\frac{4\pi}{3}(r_{\text{particle}}^3 - r_{\text{core}}^3)/V_M^B}{\frac{4\pi}{3} r_{\text{core}}^3/V_M^A + \frac{4\pi}{3}(r_{\text{particle}}^3 - r_{\text{core}}^3)/V_M^B}$$

Solving for r_{particle}, we find

$$r_{\text{particle}} = r_{\text{core}} \left(\frac{c_B/V_M^A - c_B/V_M^B + 1/V_M^B}{1/V_M^B - c_B/V_M^B} \right)^{1/3} \tag{B.1}$$

Noting that $r_{\text{core}} = r_{\text{particle}} - t_{\text{shell}}$ we can rewrite Eq. B.1 to

$$r_{\text{particle}} = \frac{t_{\text{shell}}}{1 - 1 \Big/ \left(\frac{c_B/V_M^A - c_B/V_M^B + 1/V_M^B}{1/V_M^B - c_B/V_M^B} \right)^{1/3}} \tag{B.2}$$

Conversely, we can work out the shell thickness of a core-shell nanoparticle, given its diameter and composition:

$$t_{\text{shell}} = \frac{d_{\text{particle}}}{2}\left(1 - 1\Big/\left(\frac{c_B/V_M^A - c_B/V_M^B + 1/V_M^B}{1/V_M^B - c_B/V_M^B}\right)^{1/3}\right) \tag{B.3}$$